

REFEREED CONFERENCE PAPER**Pulsed and Polarized X-ray Emission from Neutron Star Surfaces**Matthew G. Baring*¹ | Hoa Dinh Thi¹ | George Younes^{2,3} | Kun Hu⁴¹Department of Physics and Astronomy, Rice University, Houston, Texas, U.S.A.²Astrophysics Science Division, NASA's Goddard Space Flight Center, Greenbelt, Maryland, U.S.A.³CRESST, University of Maryland Baltimore County, Baltimore, Maryland, U.S.A.⁴Physics Department, McDonnell Center for the Space Sciences, Washington University in St. Louis, St. Louis, Missouri, U.S.A.**Correspondence**

*Matthew G. Baring, Department of Physics and Astronomy, Rice University, 6100 Main Street, Houston, TX 77005-1892, U.S.A. Email: baring@rice.edu

Funding Information

National Aeronautics and Space Administration, 80NSSC22K0853. 80NSSC24K0589.

The intense magnetic fields of neutron stars naturally lead to strong anisotropy and polarization of radiation emanating from their surfaces, both being sensitive to the hot spot position on the surface. Accordingly, pulse phase-resolved intensities and polarizations depend on the angle between the magnetic and spin axes and the observer's viewing direction. In this paper, results are presented from a Monte Carlo simulation of neutron star atmospheres that uses a complex electric field vector formalism to treat polarized radiative transfer due to magnetic Thomson scattering. General relativistic influences on the propagation of light from the stellar surface to a distant observer are taken into account. The paper outlines a range of theoretical predictions for pulse profiles at different X-ray energies, focusing on magnetars and also neutron stars of lower magnetization. By comparing these models with observed intensity and polarization pulse profiles for the magnetar 1RXS J1708-40, and the light curve for the pulsar PSR J0821-4300, constraints on the stellar geometry angles and the size of putative polar cap hot spots are obtained.

KEYWORDS:

stars: neutron, pulsars: general, X rays: stars, magnetic fields, diffusion

1 | INTRODUCTION

Neutron stars are the most magnetic and among the most luminous compact objects in the Milky Way. Their pulsed steady X-ray emission enables the estimation of their surface field strengths, which for **magnetars** normally exceeds 10^{14} Gauss. Soft X-ray pulsation is the telltale signature of non-uniform emission across a neutron star surface. This feature has been exploited by several groups to probe the size of the hot emission region(s), the value of the star's magnetic inclination angle α to rotation axis $\mathbf{\Omega}$ in a dipolar field morphology, and the observer's viewing direction angle ζ relative to $\mathbf{\Omega}$. For instance, Albano et al. (2010) fit the pulse profiles of the magnetar CXOU J164710.2-455216 (finding $\alpha \sim 80^\circ$ and $\zeta \sim 25^\circ$), employing blackbody emission from the whole surface, and including gravitational light bending. With a similar construct, Guillot, Perna, Rea, Viganò, and Pons (2015) found that a very small polar region with a temperature a factor of 6 larger

than the equatorial zone is required to fit the single-peaked soft X-ray profile for the "low field magnetar" SGR 0418+572. For a non-magnetar example, Gotthelf, Perna, and Halpern (2010) modeled the energy-dependent light curves of the pulsar PSR J0821-4300 in the supernova remnant Puppis A, finding that their best solution was for a quasi-orthogonal rotator viewed almost down the spin axis. Omitted from these and other similar studies are detailed treatments of local radiation anisotropy, which varies in atmospheres as the direction and magnitude of \mathbf{B} changes across the stellar surface.

X-ray polarimetry enables a new dimension in diagnostic space. *IXPE* has delivered key polarization results for four magnetars in its sensitive 2-8 keV band. For 1RXS J1708-40, the pulse profile is single-peaked at 2-4 keV energies, and the polarization degree (PD) is anti-correlated with the intensity, while the polarization angle (PA) was the same at all energies (Zane et al., 2023). This constant PA strongly contrasts the wide-ranging *IXPE* PA values seen in 4U 0142+61

⁰Abbreviations: QED: quantum electrodynamics⁰Abbreviations: *IXPE*: Imaging X-ray Polarimetry Explorer

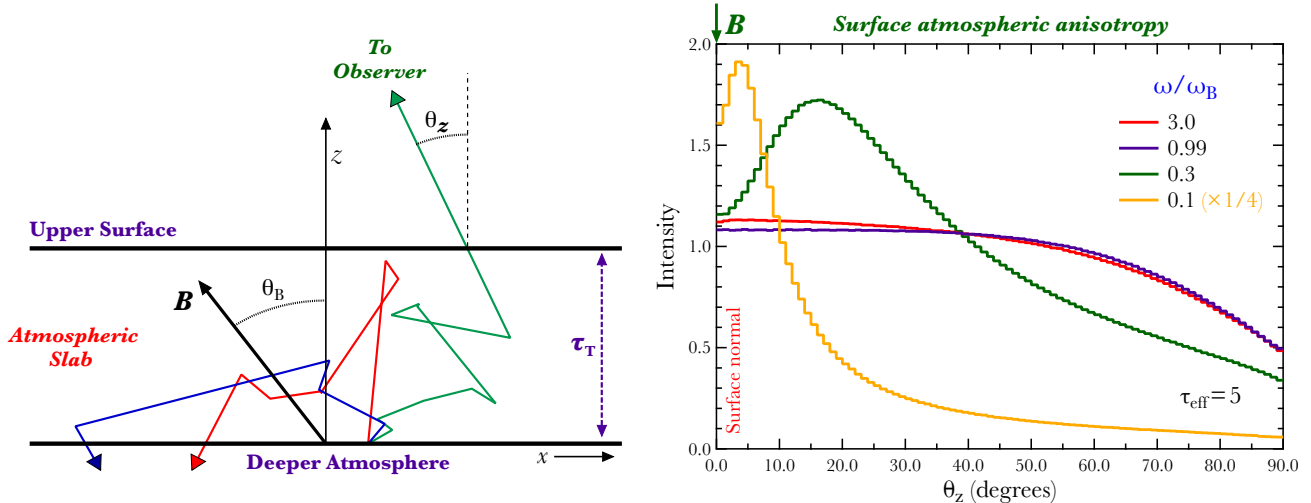


FIGURE 1 **Left:** Simulation geometry for transfer of photons through an atmospheric slab of Thomson optical depth τ_T with a normal direction along the z axis (zenith), and magnetic field putatively in the $x-z$ plane, at an angle θ_B to the local zenith. All photons emerging from the upper boundary are recorded. **Right:** Angular distributions for intensity I emergent from the top of the atmospheric slab as functions of zenith angle θ_z for runs at the magnetic pole (i.e., $\theta_B = 0^\circ$). Results are for frequency ratios $\omega/\omega_B = 0.1, 0.3, 0.99, 3$ as indicated, where ω_B is the cyclotron frequency. The effective Thomson optical depth is fixed at $\tau_{\text{eff}} = 5$. All histograms are for anisotropic and polarized injections at the slab base. Adapted from Hu et al. (2022).

between < 4 keV (where the PD is 14%) and > 5.5 keV (PD is 42%) energies (Taverna et al., 2022). The 90° PA dichotomy is perhaps most naturally interpreted as the > 5.5 keV signal emanating from a coronal region where resonant cyclotron scattering of surface photons occurs. SGR 1806-20 provided a further puzzle, with significant PD levels of 40% only in the 4-5 keV window, and less than 5% below 4 keV, leading to the suggestion (Turolla et al., 2023) that the thermal emission may originate in a condensed part of the star’s surface.

In this paper, the influences that both the anisotropy and polarization of radiation emergent from NS surfaces imprint upon their pulsed soft X-ray signals are addressed. Our tool is a high fidelity, polarized radiative transfer code that is designed for treating neutron star atmospheres. It is applied to extended surface regions, with the radiation trajectories in the magnetosphere being modified by general relativity. Intensity and PD pulse profiles for a magnetar and a low-field pulsar are explored in two case studies that illustrate the codes efficacy.

2 | MODELING ATMOSPHERIC RADIATIVE TRANSFER

The modeling of neutron star atmospheres presented in this paper uses our versatile Monte Carlo simulation named *MAGTHOMSCATT* (Barchas, Hu, & Baring, 2021; Hu et al., 2022) that tracks **polarized photon propagation and scattering** in strong fields threading atmospheric slabs. The basic slab

structure and transport schematic is shown at left in Fig. 1. The simulation models polarized magnetic Thomson opacity due to electrons in arbitrary (usually, but not necessarily uniform) magnetic field configurations for an optically thick, usually isothermal gas. It applies to both pulsars and magnetars, its structure closely resembling that of the simulation Whitney (1991) developed for white dwarf applications. The cross section is the **magnetic Thomson** one detailed in Barchas et al. (2021), which is highly anisotropic and possesses a strong dependence on photon polarization and frequency ω ; there is a profound resonance at the electron cyclotron frequency $\omega_B = eB/m_e c$. The code thus captures the intricate interplay between energy-dependent polarization and anisotropy. The code’s vertical stratification is in Thomson optical depth units, so it is simply adaptable to the atmospheric density gradients that are encountered in the hydrostatic structure.

MAGTHOMSCATT has been validated extensively (Barchas et al., 2021), reproducing anisotropic angular distributions reported by Whitney (1991) for vertical fields (\mathbf{B} is along the zenith), and non-magnetic transport characteristics detailed in the papers of Sunyaev and Titarchuk (1980, 1985). The atmospheric transport simulation yields interesting non-uniform profiles for both zenith angle and surface azimuthal angle distributions when the field direction possesses large zenith angles θ_B at quasi-equatorial surface locales. Examples of emergent radiation zenith angle distributions at the magnetic pole are provided in Fig. 1, right (from Fig. 2 of Hu et

al., 2022). These highlight the differences in anisotropy signatures at different photon energies, particularly the profound collimation/beaming of radiation near \mathbf{B} when $\omega \ll \omega_B$.

The simulation code also integrates over atmospheres covering large or complete portions of neutron star surfaces. The magnetic field is specified as a dipole configuration embedded in the Schwarzschild metric (Wasserman & Shapiro, 1983). In principle, the local temperature and brightness can be varied across the surface, although for the results presented here, they are held constant throughout the hot regions. The propagation of the additive I, Q, U, V Stokes parameters to infinity is non-dispersive and parallel-transported in the curved spacetime of the Schwarzschild metric. This metric is an appropriate choice for slowly-rotating neutron stars, i.e. excluding millisecond pulsars. The key polarization measures are the **polarization degree** (PD) Π and the **polarization angle** (PA) χ , which are given by the familiar expressions

$$\Pi = \sqrt{\left(\frac{Q}{I}\right)^2 + \left(\frac{U}{I}\right)^2}, \quad \chi = \frac{1}{2} \arctan \frac{U}{Q}. \quad (1)$$

Their values will depend on the tilt between the magnetic and rotation axes, and also the observer's viewing direction. In tracking photon \mathbf{E} -field vectors throughout the atmospheric (scattering) and magnetospheric (propagation) transport, *MAGTHOMSCATT*'s construction is designed to permit routine extension to include photon \mathbf{E} rotation in dispersive media (vacuum or plasma). It is thus prepared for future inclusion of the influences of vacuum and plasma birefringence.

3 | RESULTS

To illustrate a variety of results from our simulations of extended atmospheres, the ensuing exposition focuses on two different isolated neutron stars. The first is the magnetar 1RXS J1708-40, a bright pulsar of period 11sec, at a distance of 3.8 kpc (Olausen & Kaspi, 2014)¹; it is amenable to X-ray polarimetry using *IXPE*, due to its high spectral temperature, 0.47 keV. The second is the CCO pulsar PSR J0821-4300 in Puppis A (with period of 112 msec), which is of much lower magnetization; with its distance of 2.2 kpc and its lower effective surface temperature of 0.21 keV (Gotthelf & Halpern, 2009), it is faint enough to be difficult to measure its polarization using *IXPE*. The disparity of the spin-down fields of these pulsars underpins significant differences in their expected polarization degrees. All simulations were performed for photon propagation to infinity through a Schwarzschild metric specified by a neutron star of mass $M_{\text{NS}} = 1.44 M_{\odot}$ and radius $R_{\text{NS}} = 10^6$ cm.

3.1 | The Magnetar 1RXS J1708-40

The pulsar 1RXS J1708-40 is a prominent magnetar with a rapid spin-down (Israel et al., 1999) that leads to the inference of $B_{p,\infty} \sin \alpha = 9.3 \times 10^{14}$ Gauss using a vacuum dipole electromagnetic torque on the star. Here $B_{p,\infty}$ is its flat spacetime surface polar field strength, and α is the angle between $\boldsymbol{\mu}$ and the spin axis $\boldsymbol{\Omega}$. Its persistent pulsed emission includes quasi-thermal soft X rays below around 5 keV, with a nominal temperature of 0.45 keV (Perna, Heyl, Hernquist, Juett, & Chakrabarty, 2001; Viganò et al., 2013). This signal very likely emanates from the surface, and perhaps near its magnetic poles, with a pulse profile that varies along with its magnetospheric activity (Younes et al., 2020). It also exhibits a steady, hard X-ray tail above 10 keV (den Hartog, Kuiper, & Hermsen, 2008) that is believed to be generated by the resonant inverse Compton scattering of the surface thermal photons by relativistic electrons in the magnetosphere (e.g., Baring & Harding, 2007; Wadiasingh, Baring, Gonthier, & Harding, 2018).

1RXS J1708-40 has been well studied by a variety of X-ray telescopes over the years, and most recently by *IXPE*. The *IXPE* polarization observations (Zane et al., 2023) provide the focal point for the simulation runs that were completed in studying this magnetar and present here. Specifically, the 2-8 keV *IXPE* spectrum can be fit by both two blackbody (BB+BB, hot and cold) and blackbody plus power-law (BB+PL) superpositions. The intensity pulse profile is single-peaked in the softer 2-4 keV band, and moreover the polarization degree Π is anti-correlated with the intensity. These characteristics are displayed in Fig. 2. The phase-averaged polarization angle χ , displayed in Fig. 1 of Zane et al. (2023), was roughly the same at all energies in the 2-8 keV band.

To model this data, a number of simulations at different frequency ratios ω/ω_B were performed. This ensemble encompassed a range of frequencies appropriate to match the 2–4 keV *IXPE* dataset, and accommodate surface atmospheres with a polar field of 9.3×10^{14} Gauss, as perceived by an observer at infinity. They were weighted by a Planck spectrum of temperature $kT \sim 0.47$ keV. The resulting photon energy ranges, as appreciated by an observer at infinity, are listed in the panel headers in Fig. 2. These increase by a factor of 1.32, the inverse of the gravitational redshift factor $\sqrt{1 - 2GM_{\text{NS}}/(R_{\text{NS}}c^2)} \approx 0.76$, when measured in the local inertial frame at the stellar surface. There are three main geometrical parameters, $\alpha = \arccos \hat{\boldsymbol{\mu}} \cdot \hat{\boldsymbol{\Omega}}$, the viewing angle ζ to the spin axis $\boldsymbol{\Omega}$, and the colatitudinal extent θ_{cap} of each antipodal polar cap. The solid angle-integrated emissivity is uniform across the cap. The goal is to constrain their values using the intensity and polarization degree light curves.

To do this, the data of all photons emitted from two identical antipodal surface polar caps to all directions on the sky is binned into observer angle cones of opening half-angle ζ and

¹For a comprehensive summary of magnetar properties, see the McGill Online Magnetar Catalog at <http://www.physics.mcgill.ca/pulsar/magnetar/main.html>

¹**Abbreviations:** CCO: central compact object

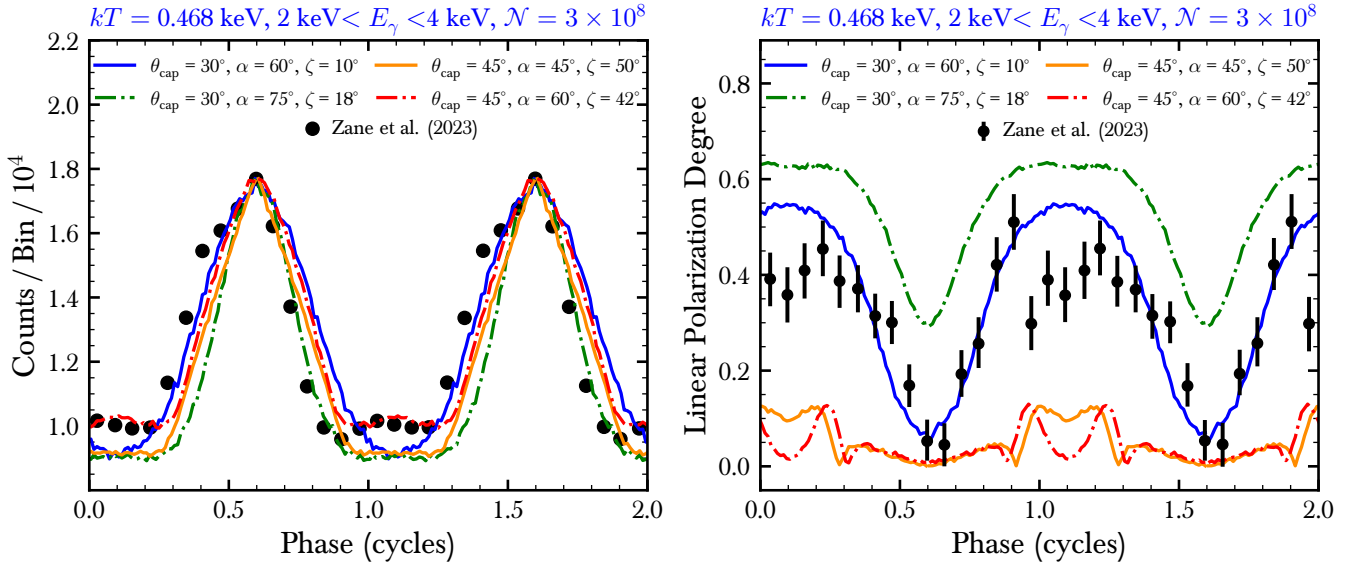


FIGURE 2 Simulated soft X-ray pulse profiles from *MAGTHOMSCATT* for intensity I (left) and polarization degree (PD) Π (right) for two antipodal polar caps extending from the respective magnetic poles to colatitudes of $\theta_{\text{cap}} = 30^\circ, 45^\circ$, as labelled. The points are *IXPE* data from Fig. 4 of Zane et al. (2023) for the persistent 2-4 keV emission of the magnetar 1RXS J1708-40. The different (α, ζ) choices (see text) on the left all approximately describe the observed *IXPE* light curve. For the corresponding Π at right, the models do not include the influences of vacuum birefringent propagation of light through the magnetosphere.

then sub-divided into bins of azimuthal angles around the spin axis Ω , which then constitute different rotational pulse phases $\Phi = \Omega t$. The products are two-dimensional (2D) “sky maps” of intensity and polarization information in the $\Omega t - \zeta$ plane, for each magnetic inclination angle α , which is increased in 5° increments. Examples of such sky maps are given in Figs. 4 and 5 of Hu et al. (2022). Horizontal cuts of such 2D maps then select light curves for a full range of values for ζ , again incremented in 4° intervals.

These light curves were then compared with the *IXPE* intensity data, normalized so that the peaks coincide with those of the data. Using a visual inspection of a myriad of light curves (a χ^2 statistical analysis was not possible due to the small error bars), the best “fitting” four pulse profiles are displayed in Fig. 2 (left) for two polar cap sizes, $\theta_{\text{cap}} = 30^\circ, 45^\circ$. These are clearly not good statistical fits, just general indications. The symmetry of our dual polar cap constructions necessarily yields symmetric peaks and valleys in the light curves. In contrast, the data possess a skewness that indicates surface non-uniformities in the emissivity; addressing such surface variations in detail is beyond the scope of this work. The four models suggest a strong preference for an oblique rotator, with the magnetic inclination ranging from $\alpha = 45^\circ$ to $\alpha = 75^\circ$. Taken at face value, this would suggest a bound $9.6 \times 10^{14} \text{ Gauss} < B_{p,\infty} < 1.3 \times 10^{15} \text{ Gauss}$. Note that in principle, one should adjust the photon energy range for each inferred α , yet in practice, this protocol would make for only a

small difference in the model fitting parameter estimation. The range of possible viewing angles ζ is also quite large.

The discrimination between these four best cases can be helped by inspection of the corresponding PD pulse profiles (which are not fits), displayed on the right of Fig. 2. Therein, the two cases with cap sizes $\theta_{\text{cap}} = 45^\circ$ are strongly depolarized due to the large range of field directions spanned across the cap. This depolarization trend is apparent when comparing the sky maps in Figs. 6 and 7 of Hu et al. (2022). The $\alpha = 60^\circ, \zeta = 10^\circ$ example in Fig. 2 gives the best broad brush fit to the PD light curve. However, this result was obtained with just the simple general relativistic parallel transport of photon polarization vectors in the magnetosphere. Therefore, our results did not include the role of QED magnetic vacuum birefringence on the transport of polarizations to infinity; it preserves the polarization eigenstates and drive the net polarization degree much higher (Heyl & Shaviv, 2000). This influence is detailed in Dinh Thi et al. (in prep.), wherein PDs above 0.8 are routinely realized for 1RXS J1708-40 using the same atmosphere output detailed here. Neither does our modeling include the competition between vacuum and plasma birefringence within the atmosphere, an influence that depolarizes surface signals overall (Lai & Ho, 2003), partially compensating the magnetospheric birefringence effects. Accordingly, future enhancements of our models including these influences will provide an improved picture of polarization predictions that would be better suited to *IXPE* magnetar data comparison.

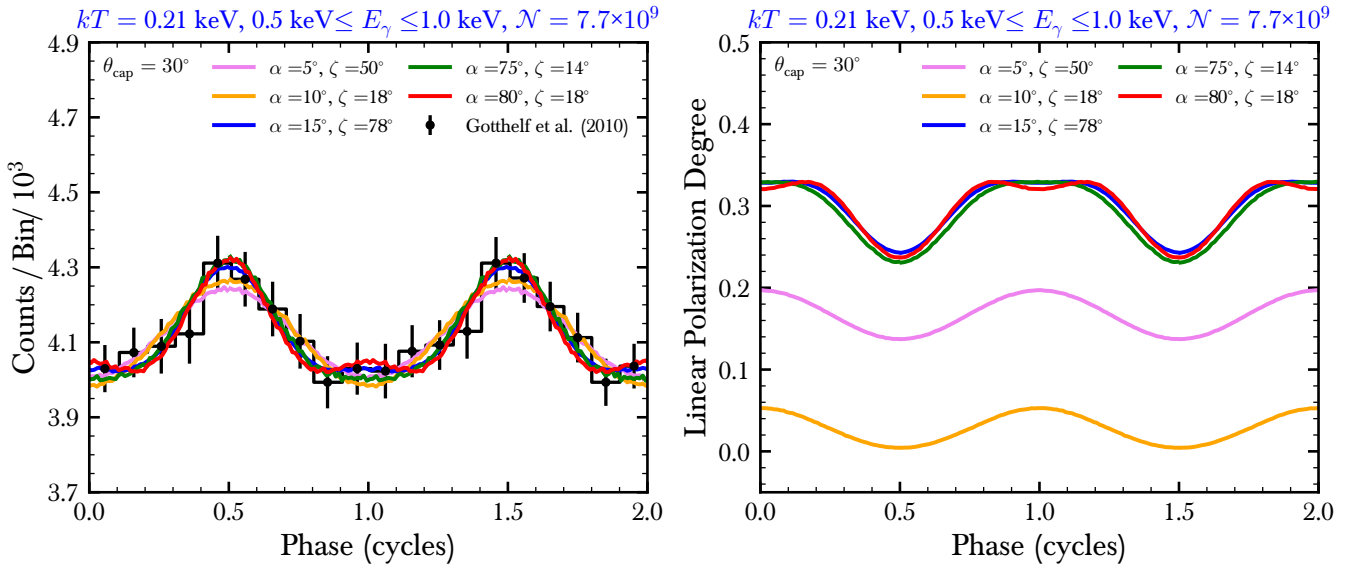


FIGURE 3 Simulated soft X-ray pulse profiles from *MAGTHOMSCATT* for intensity I (left) and polarization degree (PD) Π (right) for the CCO pulsar J0821-4300 (see text). The two antipodal polar caps extend from the respective magnetic poles to colatitudes of $\theta_{\text{cap}} = 30^\circ$. The intensity data (left) are from the persistent 0.5-1 keV pulse profile displayed in Fig. 5 of Gotthelf et al. (2010). The different (α, ζ) choices on the left all approximately describe the observed *XMM-Newton* light curve. For the corresponding Π at right, some of the models indicate the potential of polarimetry to help break parameter degeneracies.

3.2 | The CCO Pulsar PSR J0821-4300

Our second case study is for PSR J0821-4300 (more recently designated J0822-4300 due to its proper motion), an isolated neutron star of much lower magnetization. Sometimes dubbed an “anti-magnetar,” its discovery did not permit a measurable period derivative \dot{P} at first (Gotthelf & Halpern, 2009), though when eventually secured at $\dot{P} = 9.3 \times 10^{-18}$, it led to the spin-down inference of $B_{p,\infty} \sin \alpha = 5.7 \times 10^{10}$ Gauss for a vacuum rotator in flat spacetime (Gotthelf, Halpern, & Alford, 2013). Another special aspect to its character is its low pulsation amplitude (pulse fraction), around 8%, contrasting the large intensity modulation for 1RXS J1708-40 discernible in Fig. 2. Interestingly, the peak in the pulse profiles changed phase by 180° between energies below 1.2 keV and those above this value (Gotthelf & Halpern, 2009). This feature was explained by Gotthelf et al. (2010) as signifying one polar cap being much hotter than the other.

To explore how the light curves for this CCO pulsar can constrain the surface emission geometry, a similar protocol as in Sec. 3.1 is adopted. The intensity pulse profile that will be focused upon is that obtained from *XMM-Newton* observations below 1 keV, and is displayed in Fig. 3, left. The geometry will be two identical temperature, antipodal polar caps extending from the magnetic poles out to magnetic colatitudes $\theta_{\text{cap}} = 30^\circ$ distant. This contrasts the set-up in Gotthelf et al. (2010), wherein the two poles were of different sizes and temperatures. Such an extension with our *MAGTHOMSCATT*

simulation is deferred to a future study, where its implications can be explored at length. Here, a general sense of what the stellar geometric parameters $\alpha = \arccos \hat{\mu} \cdot \hat{\Omega}$ (magnetic inclination) and viewing angle ζ are likely to be is posited.

Again, a number of simulations was performed at different frequency ratios ω/ω_B that bracket the thermal photon energies pertaining to a temperature of around 0.21 keV. In the local inertial frame (LIF) at the surface, the gravitational redshift yields an increase in T_{eff} by $1/\sqrt{1 - 2GM_{\text{NS}}/(R_{\text{NS}}c^2)} \approx 1.32$. These frequency results were then weighted with the appropriate Planck function. The polar field strength as perceived at infinity was 5.7×10^{10} Gauss, which increases to 8.5×10^{10} Gauss in the LIF at the surface. Again, the data of all photons emitted from a uniformly-emitting surface polar cap to all directions was binned into observer angle cones of opening half-angle ζ (in 4° intervals) around the spin axis Ω . Thus 2D “sky maps” of intensity and polarization information in the $\Omega t - \zeta$ plane were generated for each rotator inclination angle α that was stepped incrementally by 5° . Horizontal cuts of such 2D maps then generated the pulse profiles illustrated in Fig. 3.

Of the multitude of resulting pulse profiles, five best fit models are illustrated in Fig. 3. Not all pulse profiles that were derived from the sky maps had pulse fractions this small. These preferred models were determined using a χ^2 statistics minimization approach when assuming Gaussian errors in the displayed PSR J0821-4300 counts (intensity) data. Both small

and large α were permissible, and similarly smaller and large ζ could be possible. In the small $\alpha = 5^\circ, 10^\circ, 15^\circ$ examples, the remote polar cap is barely visible to an observer, so the peak at phase 0.5 is due to the proximate polar cap. For the large α profiles, both caps are visible, yet the small observer inclination to the spin axis reduces the pulse fraction.

Discriminating between these geometry parameters using polarimetry is unfortunately not possible, since the low temperature renders PSR J0821-4300 a low flux target that proves difficult for *IXPE* to successfully measure polarizations for. Nevertheless, PD traces were also generated, on the right of Fig. 3, to provide a general sense of what might be probed by a future, more sensitive X-ray polarimeter. Again, these are generated using parallel transport of photon electric field vectors in the Schwarzschild metric, from the stellar surface to infinity.

The polarization degrees overall are much lower than those for 1RXS J1708-40. This is principally because of the much lower magnetization. The electron cyclotron energy in the local inertial frame is given by

$$E_{\text{cyc}} = \hbar\omega_{\text{B}} = \frac{e\hbar B}{m_e c} = 11.6 \frac{B}{10^{12} \text{G}} \text{ keV}. \quad (2)$$

This sets up at 0.66 keV for PSR J0821-4300 in the observer frame, right in the energy range of interest below 1 keV in Fig. 3. Thus the scattering in the atmosphere is around the cyclotron frequency, a domain in which the linear/circular polarization modes all have similar magnetic Thomson cross sections: see Barchas et al. (2021). This leads to modest overall polarization degrees, even for $\theta_{\text{cap}} = 30^\circ$. This contrasts the magnetar case, where $\omega \ll \omega_{\text{B}}$ always, and there is a strong dominance of the \parallel linear mode (O-mode) over the \perp one (X-mode), with minimal circular polarization. This one-sidedness drives the net PD up to the large values evident here.

While the PD information separates off two cases as they have PD values inferior to 0.2, it is clear that three cases are essentially indistinguishable. However, it was found that by isolating individual Stokes Q and U information via the polarization angle χ in Eq. (1), the $\alpha = 15^\circ, \zeta = 78^\circ$ case can be separated from the other two (not shown here). Thus one has a path to constraining the α, ζ parameter space to around 10° in a future advanced polarimetry era. Notwithstanding, it should again be mentioned that the PD levels do rise substantially when the effects of vacuum birefringence on the polarization modes throughout magnetospheric propagation is taken into account (Dinh Thi et al., in prep.).

4 | CONCLUSION

This paper has presented sample results from our magnetic Thomson radiative transfer code *MAGTHOMSCATT* that models atmospheres of neutron stars of various magnetizations. The polarized, anisotropic signals are then propagated in

curved spacetime through the magnetosphere to infinity. The case studies presented here illustrate how our simulation data can be applied to both a magnetar and an isolated, low-field pulsar to constrain key stellar geometry parameters, and the spatial extent of the emitting surface. While light curve modeling efforts have been delivered before, our program brings greater depth to this approach through its precision simulation of atmospheric anisotropies and polarizations, and their coupling to magnetic colatitudes. Thus, it is well positioned to interpret the X-ray polarization data being delivered by *IXPE*.

ACKNOWLEDGMENTS

This work was performed with the support of the **National Aeronautics and Space Administration** under Grant Nos. *80NSSC22K0853* and *80NSSC24K0589*.

REFERENCES

- Albano, A., Turolla, R., Israel, G. L., Zane, S., Nobili, L., & Stella, L. (2010), *ApJ*, 722, 788-802.
- Barchas, J. A., Hu, K., & Baring, M. G. (2021), *MNRAS*, 500, 5369-5392.
- Baring, M. G., & Harding, A. K. (2007), *Astr. Space Sci.*, 308, 109-118.
- den Hartog, P. R., Kuiper, L., & Hermsen, W. (2008), *A&A*, 489, 263-279.
- Gotthelf, E. V., & Halpern, J. P. (2009), *ApJ*, 695, L35-L39.
- Gotthelf, E. V., Halpern, J. P., & Alford, J. (2013), *ApJ*, 765, 58.
- Gotthelf, E. V., Perna, R., & Halpern, J. P. (2010), *ApJ*, 724, 1316-1324.
- Guillot, S., Perna, R., Rea, N., Viganò, D., & Pons, J. A. (2015), *MNRAS*, 452, 3357-3368.
- Heyl, J. S., & Shaviv, N. J. (2000), *MNRAS*, 311, 555-564.
- Hu, K., Baring, M. G., Barchas, J. A., & Younes, G. (2022), *ApJ*, 928, 82.
- Israel, G. L., Covino, S., Stella, L., Campana, S., Haberl, F., & Mereghetti, S. (1999), *ApJ*, 518, L107-L110.
- Lai, D., & Ho, W. C. G. (2003), *ApJ*, 588, 962-974.
- Olausen, S. A., & Kaspi, V. M. (2014), *ApJS*, 212, 6.
- Perna, R., Heyl, J. S., Hernquist, L. E., Juett, A. M., & Chakrabarty, D. (2001), *ApJ*, 557, 18-23.
- Sunyaev, R. A., & Titarchuk, L. G. (1980), *A&A*, 86, 121-138.
- Sunyaev, R. A., & Titarchuk, L. G. (1985), *A&A*, 143, 374-388.
- Taverna, R., Turolla, R., Muleri, F. et al. (2022), *Science*, 378, 646-650.
- Turolla, R., Taverna, R., Israel, G. L. et al. (2023), *ApJ*, 954, 88.
- Viganò, D., Rea, N., Pons, J. A., Perna, R., Aguilera, D. N., & Miralles, J. A. (2013), *MNRAS*, 434, 123-141.
- Wadiasingh, Z., Baring, M. G., Gonthier, P. L., & Harding, A. K. (2018), *ApJ*, 854, 98.
- Wasserman, I., & Shapiro, S. L. (1983), *ApJ*, 265, 1036-1046.
- Whitney, B. A. (1991), *ApJS*, 75, 1293-1322.
- Younes, G., Baring, M. G., Kouveliotou, C., Wadiasingh, Z., Huppenkothen, D., & Harding, A. K. (2020), *ApJ*, 889, L27.
- Zane, S., Taverna, R., González-Caniulef, D. et al. (2023), *ApJ*, 944, L27.

